Heliyon 8 (2022) e11459

Contents lists available at ScienceDirect

Heliyon

journal homepage: www.cell.com/heliyon

Research article

Oxidation state, local structure distortion, and defect structure analysis of Cu doped α-MnO_2 correlated to conductivity and dielectric properties

E. Hastuti [a,b], A. Subhan [c], P. Amonpattaratkit [d], M. Zainuri [a], T. Triwikantoro [a], S. Suasmoro [a,*]

[a] Institute of Technology 'Sepuluh Nopember' Surabaya, Kampus ITS Sukolilo, Surabaya 60111, Indonesia
[b] Universitas Islam Negeri 'Maulana Malik Ibrahim' Malang, Indonesia
[c] Research Centre for Physics, Indonesian Institute for Science (LIPI), Serpong, Indonesia
[d] Synchrotron Light Research Institute (Public Organisation), 111 University Avenue, Muang, Nakhon Ratchasima 30000, Thailand

ARTICLE INFO

Keywords:
Manganese dioxide
Doping
Oxidation state
Local distortion
Defect structure

ABSTRACT

Cu-doped MnO_2 with the composition of $Mn_{1-x}Cu_xO_2$ (x = 0–0.15) was synthesized and characterized. The synthesis was carried out by hydrothermal method at 140 °C for 5 h of reaction dwell time. The characterizations include X-Ray Diffraction (XRD), Microscopy, X-ray Absorption Spectroscopy (XAS), and Impedance complex analysis. It was revealed that all samples have nanorod morphology. Their size increases with the increasing dopant. Additionally, K ions are detected by EDX. All samples pose α-MnO_2 type structures performing (2 × 2) and (1 × 1) tunnels permitting large ions incorporated and oxygen deficiency. The octahedron was distorted to elongate up to x = 0.10, then compressed for x = 0.15, inducing the Jan Teller effect. Oxidation state analysis revealed that the manganese has Mn^{3+} and Mn^{4+}, while the copper is mainly attributed to Cu^{2+} and Cu^{3+} respectively. The small ionic size and highly oxidized Cu^{3+} substitute Mn^{4+}, while Cu^{2+} substitutes Mn^{3+} or simultaneously with the larger K^+ incorporated in the tunnel. Accordingly, the defects to exist in the sample, namely Cu'_{Mn}, Mn'_{Mn}, $V_O^{\bullet\bullet}$, and e'. Electrical characterization at room temperature revealed that the conductivity of Cu-doped MnO_2 is dominated by electrons influenced by the various oxidation state of the cations in the octahedron sites, while space charges dominate the dielectric response.

1. Introduction

Research on energy storage for various applications in recent years has existed in four categories, *i.e.,* mechanics, chemical, electrical and electrochemical [1]. Electrochemical energy storage (EES) has shown great potential in portable electrical energy storage, efficient, long-life cycle, and potentially implemented by cheap chemical material, renewable and low maintenance such as supercapacitors, batteries, and fuel cells [2]. The energy storage principles in supercapacitors are based on the charge-discharge mechanism between electrolyte and electrode, and the storage capacity is much higher than the conventional capacitor. It can reach 100 mF–1000 mF and possesses an energy density several times higher than the battery [3].

Various supercapacitor development has been carried out, including carbon and oxide-based materials. The carbon-based comprises carbon nanotubes (CNTs), activated carbon, carbon black, carbon fiber, and graphene [4, 5, 6, 7], whereas the oxide-based includes NiO, MoO, Co_2O_3, IrO_2, FeO, TiO_2, SnO_2, V_2O_3, MnO_2 [8] and RuO_2 [9]. The MnO_2 was reported to have a high theoretical specific capacitance of 1300 F g^{-1}. However, in most applications, the electrochemical reversibility of the redox transition is low, and pure MnO_2 has a poor capacitive response and a high resistance [10]. Besides these, manganese oxide is a potentially valuable material for supercapacitors because of its low cost, large quantity, and non-toxicity [8].

Given the structure, manganese dioxide is built from a basic [MnO_6] octahedron unit that forms corner-shared and edge-shared links each other and exhibits various crystal structures, including α-MnO_2, β-MnO_2, γ-MnO_2, δ-MnO_2, λ-MnO_2, ε-MnO_2, and R–MnO_2 [11]. The crystalline structure is one of the determinant factors related to the properties and optimizing MnO_2 as supercapacitor material. The MnO_2-based electrode stores an electric charge by a pseudocapacitive mechanism [12]. The charge storage is initiated from the Mn oxidation state in 3+/4 + at or near the surface of the MnO_2 nanostructure [13]. The adsorption/desorption of electrolyte ions and protons on the MnO_2 surface causes a

* Corresponding author.
E-mail address: suasm@its.ac.id (S. Suasmoro).

https://doi.org/10.1016/j.heliyon.2022.e11459
Received 17 August 2022; Received in revised form 28 September 2022; Accepted 2 November 2022

surface faradaic reaction [14]. Additionally, the bulk pseudocapacitive response depends on the intercalation-deintercalation of protons or cations into most of the MnO_2 [12].

Defects creations are well-known as a strategy to improve the electronic properties of the materials comprising MnO_2. Various cations doped were reported to create defects such as Zn, Co, Ni, Ca, Fe, Al, Mg, and Cu [15, 16, 17]. Al^{3+} was reported to induce phase transformation of MnO_2 nanoparticles from α to β and revealed absorption towards the visible light region [17]. While in Fe, Co, and Ni-doped MnO_2 nanosheets are observed, indicating a hexagonal unit cell and the layered Birnessite-type structure (δ-MnO_2) [16]. Similarly, Cu doped was reported to have an δ-MnO_2 type structure [18] and intercalated MnO_2 about the narrowing of bandgap and enhancing charge mobility during catalysis. Fu [19] found that in the nanowires Cu–MnO_2, the mixed oxidation state Cu^{+}/Cu^{2+} and Mn^{3+}/Mn^{2+} exhibited the highest specific capacitance of 921 F/g at the current density of 1 A/g. α-MnO_2 shows excellent catalytic activity with very high capacity and stable cycling than layered Birnessite δ-MnO_2 for electrochemical application [20]. It is intriguing to deeper analysis to explore the material aspect and the mechanism related the properties.

Besides, various synthesis methods were reported, including co-precipitation [21], electrochemical deposition [22], sol-gel, and hydrothermal [23]. The hydrothermal process is the most preferred approach to synthesizing MnO_2 due to its simplicity, good repeatability, and high reliability [24]. Zhao [25] synthesized MnO_2 through hydrothermal and varies the experimental variables, reaction time, pH, and doping percentage, to attain α-MnO_2, β-MnO_2, and δ-MnO_2 when the ratio of $MnSO_4.H_2O/KMnO_4 = 1/1$, 3/2, and 3/8 was made. When the Cu dopant is taken, it becomes noteworthy since Cu is a metal transition possessing a 3d sub-shell with multivalence 1+, 2+, and 3+ [26]. Various studies on transition metal doping on Mn have been carried out [15]. However, the mechanism of substitution and interstitial dopant atoms in MnO_2 has lacked discussion as well as the changes in oxidation number due to doping.

X-ray absorption spectroscopy (XAS) is a straightforward, reliable, and widely used technique for identifying and quantifying various chemical species. The X-ray absorption near edge structure (XANES) energy relates to the excitation of electrons and obeys the selection rule. This absorption energy is sensitive to the oxidization state and electronic structure of the detected elements as the core electron energy and is affected by the electron distribution in the valence state [27]. At the XANES region, the metal transition K-edge absorption corresponds to the dipole transition from the 1s to 4p states, while the pre-edge includes the quadrupole transition from the 1s to 3d which split into e_g and t_{2g} states and is related to the valence of the absorber.

While the extended X-ray absorption fine structure (EXAFS) is a powerful means to determine the local structure around the absorbing atom, comprising bond distance, coordination number, and chemical identity of the elements [28]. At the EXAFS energy, the ejected photoelectrons are excited into a continuum that is dominated by electron scattering, which is related to the absorption process. Photoelectron waves that are released and scattered will interfere with one another. The interference pattern formed is determined by the path length of the two waves, and as a result, the pattern provides information about the local structure surrounding the absorbing atom. The equation can be applied to describe EXAFS [29].

$$\chi(k) = \sum_j \frac{N_j f_j(k)\, exp\left[-2k^2\sigma_j^2\right]\, exp\left[-2R_j/\lambda\right]}{kR_j^2}\, sin\left[2kR_j + \delta_j(k)\right] \quad (1)$$

Where k is the photoelectron wave number, N is the number of neighboring atoms, R is the distance from the absorber atom, $f(k)$ and $\delta(k)$ are the current scattering factors of atoms neighboring the excited atom, and σ^2 is the mean square displacement in R. The EXAFS equation can be used to calculate the number and distances of neighboring atoms and the disorder in this distance after the scattering factors $f(k)$ and $\delta(k)$ are known [30].

In the previous studies [31, 32], X-ray Absorption Spectroscopy (XAS) has been exploited to determine the oxidation state of Cu/Fe in the octahedron environment, furthermore, extended X-ray Absorption Fine Structure (EXAFS) was exploited for local structure studies. Hence it is essential to explore using a similar method, the nature of defects, the oxidation state of cations in the synthesized material, and whether Cu will substitute Mn in the octahedron or occupy MnO_2 tunnels.

The doping process is expected to reveal the role of fundamental structural variables in affecting the conductivity, permittivity, and capacitance of materials; therefore, a keen analysis is then performed to elucidate the phenomena. In this study, α-MnO_2 was synthesized with various percentages of Cu doping using the hydrothermal method. Furthermore, to determine the changes in α-MnO_2 due to doping: phase, crystallite size, microstrain, defects, changes in atomic positions (lattice distortion), oxidation state, and microstructural analysis.

2. Materials and methods

2.1. Materials preparation

$Mn_{1-x}Cu_xO_2$ (MCx) nanorods were synthesized using an autoclave hydrothermal method (Teflon liner, 100 mL capacity). First, $KMnO_4$ (0.526 g, 3.32 mmol) was dissolved in 60 mL of demineralized water at room temperature, then concentrated HCl (37%, 2.39 mmol) was added to the solution batch. Second, the Cu dopant reagent's $CuCl_2{\cdot}2H_2O$ was used and weighted to desired percentage [0 (0.0283 g, 5 mol %) (0.0566 g, 10 mol %) and (0.0849 g, 15 mol %)]. These dopant reagents were added to each batched solution above to achieve MnO_2 with different copper doping levels. Third, each mixture batch was then heated to 140 °C and held for 5 h to ensure the formation of α-MnO_2 phase nanorods [33]. Upon completion, all reactions were cooled to room temperature. The solids were washed with demineralized water and ethanol several times and dried in an oven at 80 °C for 3 h.

2.2. Characterization

X-ray diffraction (XRD Philips X'Pert) was employed to investigate the phase and crystal structure MnO_2 with Cu-Kα radiation operated at 30 mA and 40 kV, step scan 0.02°, and Bragg angle range from 10° to 70°. Phase identification was accomplished through the match! Software, while the lattice parameters were inferred using Rietveld's refinement based on the α-MnO_2 model structure (JCPDS file 00-44-0141).

The morphology was determined by the Field Emission Scanning Electron Microscope (FESEM) image and other elements maps involved energy-dispersive X-ray (EDX) analysis. The numerical dimension of each sample was obtained by averaging the diameters of nanorods from different samples using ImageJ software [34]. Transmission electron microscopy (TEM, Tecnai G2 20 S-Twin) and high-resolution transmission electron microscopy (HRTEM) further characterize the crystal structure details with STEM_CELL software [35]. CrysTBox software [36] recorded and analyzed selected area electron diffraction (SAED) patterns to obtain d spacing.

The X-ray absorption near edge structure (XANES) and extended X-ray absorption fine structure (EXAFS) of Mn–K edge and Cu–K edge were studied at the Synchrotron Light Research Institute's beamline BL-8 (SLRI). All spectra were collected in transmission mode at room temperature using an energy range of 1.25–10 keV. The data obtained were calibrated and normalized using Athena software. Analysis of the interatomic distance in the local structure, using the Artemis software on IFEFFIT with the match parameters R-factor, distribution amplitude (S_0^2), and Debye-Waller factor (σ^2) [37]. The structural model used in the fitting process is α-MnO_2 with a fixed coordination number (CN) to obtain amp, then used to determine CN and R-space with the same FT.

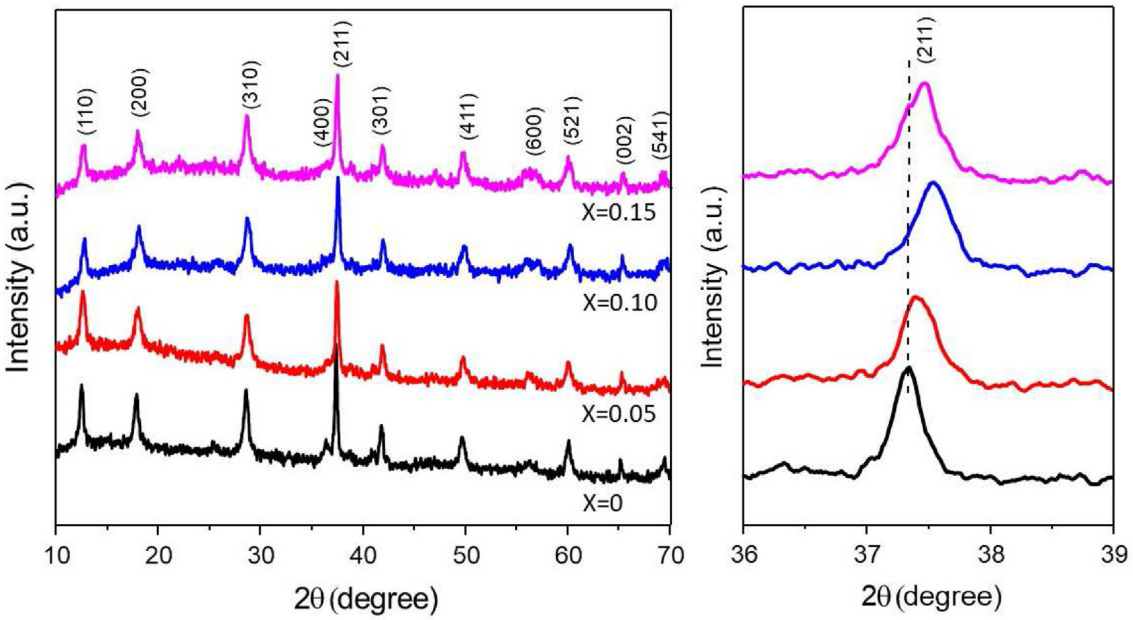

Figure 1. XRD pattern of MCx samples (left), the enlargement of diffraction peaks at 2Θ ≈37-38° (right).

Dielectric and electrical conduction measurements were performed on powder inserted between two copper electrodes and then uniaxially pressed at ≈ 0.4 MPa with a diameter of 13 mm. The acquisition data was acquired using Solartron Impedance Analyzer SI 1260 in the frequency range of 0.1 Hz–32 MHz, and 1 V applied voltage at room temperature.

3. Results and discussions

3.1. Microstructure and structure analysis

3.1.1. Powder diffraction

Figure 1 shows the XRD patterns of Cu-doped MnO_2 ($Mn_{1-x}Cu_xO_{2-\delta}$, x = 0–0.15 hereafter abbreviated MCx) as-synthesized powder. It displays considerable similarities, and there is no typical phase related to Cu, and its oxides nor other impurities were detected. All the diffraction peaks can be indexed to the tetragonal structure of α-MnO_2 (JCPDS 44–0141) and *I4/m* symmetry. It behaves edge-sharing (e-s) and corner-sharing (c-s) [MnO_6] octahedrons, leading to the formation of (2 × 2) and (1 × 1) tunnels. However, in the Cu-doped samples, the diffraction peaks slightly shift to a higher diffraction angle up to x = 0.10, then move back to a lower position, Figure 1 enlargement peaks. This phenomenon implies the shortened lattice parameter following the Bragg diffraction rule. Given that the ionic radii of Cu^{2+} and Cu^{+} (73 and 77 pm) are more significant than Mn^{4+} or Mn^{3+} (53 and 64.5 pm), which coexist in the MnO_2 [33], consequently, the Cu^{+} and Cu^{2+} are unexpected to replace Mn^{4+} in octahedron [MnO_6] readily, alternatively, the possible occurrence when Mn in lower oxidation state such as Mn^{2+} (83 pm). If Cu^{2+} substitutes Mn^{3+}, the lattice parameter will increase, and the diffraction peaks shift to a lower angle, contrary to the diffraction data in Figure 1. These contrasting results point out that another cause may exist. A possible reason should be addressed that lattice electric field interaction lowered the total energy of ionic interaction, increasing Coulombic attraction when copper substituted Mn as indicated in $Ba_{0.5}Sr_{0.5}TiO_3$ doped $K_{0.5}Na_{0.5}NbO_3$ system [38]. Besides, Cu^{+} and Cu^{2+} may occupy a tunnel in the α-MnO_2 structure. Therefore, based on ionic radii, a possible substitution of copper in manganese occurs when the oxidation state of copper is 3 + possessing a radius of 54 pm, further analysis will be provided in § 3.2 and § 3.3. Incorporating Cu^{3+} ions into the α-MnO_2 structure may modify the lattice parameters, crystallite size, and micro-strain. Further refinement analysis to quantify those parameters is listed in Table 1.

The lattice parameters values presented in Table 1 indicate that the shortening of crystal parameters occurred both in the a/b and c-axes direction when the Cu doping increased up to x = 0.10 and then re-expanded for x = 0.15. The possible cause is the number of interstitial Cu^{+}/Cu^{2+} ions in the tunnel or the substitution of Cu^{3+} ions to Mn in the octahedral structure of α-MnO_2. Furthermore, the crystalline size in this analysis was determined through peak broadening analysis following the Scherrer formula ($t = 0.9\lambda/B\cos\theta$) resulting in scattered values following doping percentage. The average crystalline size is 26.55 nm for an undoped sample, 22.81 nm, 25.02 nm, and 25.68 nm for the Cu-doped sample with concentrations x = 0.05, 0.10, 0.15. However, it has an increasing tendency with doping except for the undoped. The possible cause should be addressed to the validity of the Scherrer formula which is limited to the small size (<100 nm) particles as well as rounded crystalline morphology [39]. Further direct determination is presented in the following paragraph through FESEM and TEM analysis.

Table 1. Rietveld's refinement results for MCx samples, the related crystalline size, and the microstrain are indicated.

Sample	Reliability factor R_{wp} (%)	a = b (Å)	c (Å)	Volume (Å)^3	Crystallite size (*) (nm)	Micro strain (x10^{-3})
x = 0	7.078	9.8614 ± 0.0017	2.8686 ± 0.0005	278.9633	26.55	1.42
x = 0.05	7.105	9.8453 ± 0.0018	2.8639 ± 0.0006	277.6098	22.81	1.92
x = 0.10	6.538	9.8287 ± 0.0024	2.8585 ± 0.0008	276.1496	25.02	1.60
x = 0.15	6.219	9.8472 ± 0.0026	2.8625 ± 0.0006	277.3253	25.68	1.52

(*) determined through the Debye-Scherer method.

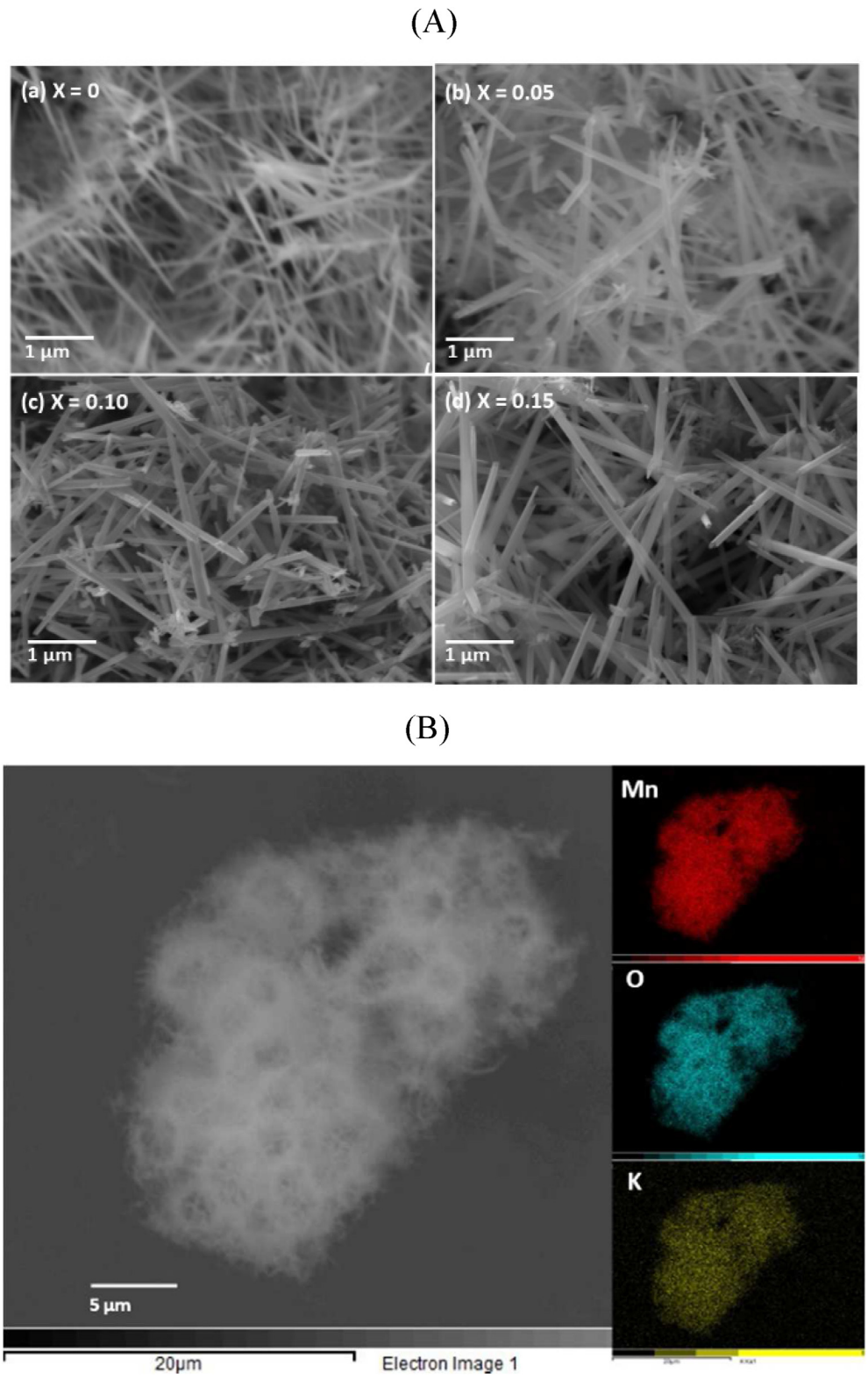

Figure 2. (A) FESEM image of nanorods MCx samples (B) EDX mapping of MC0 sample.

3.1.2. *Microscopic analysis*

The SEM image in Figure 2A(a) indicates the MC0 sample comprised of nanorods morphology possessing a diameter of about 54 nm and 2 µm long, determined through ImageJ software. While the Cu-doped MnO_2 poses a larger diameter and increases with the amount of Cu (Figure 2A(b-d)), the measured diameters are around 69, 98, and 107 nm for x = 0.05, 0.10, and 0.15, respectively. The energy dispersive spectroscopy (EDS) mapping in Figure 2B shows that K^+ ions spread evenly, while other elements Mn and O are similarly distributed in the sample.

TEM measurements of MCx nanorods are shown in Figure 3 (a-1, b-1,c-1, d-1), with an average diameter of about 54, 69, 90, and 110 nm for x = 0, 0.05, 0.10, and 0.15, respectively. This result is similar to the diameter in the FESEM analysis described previously. However,

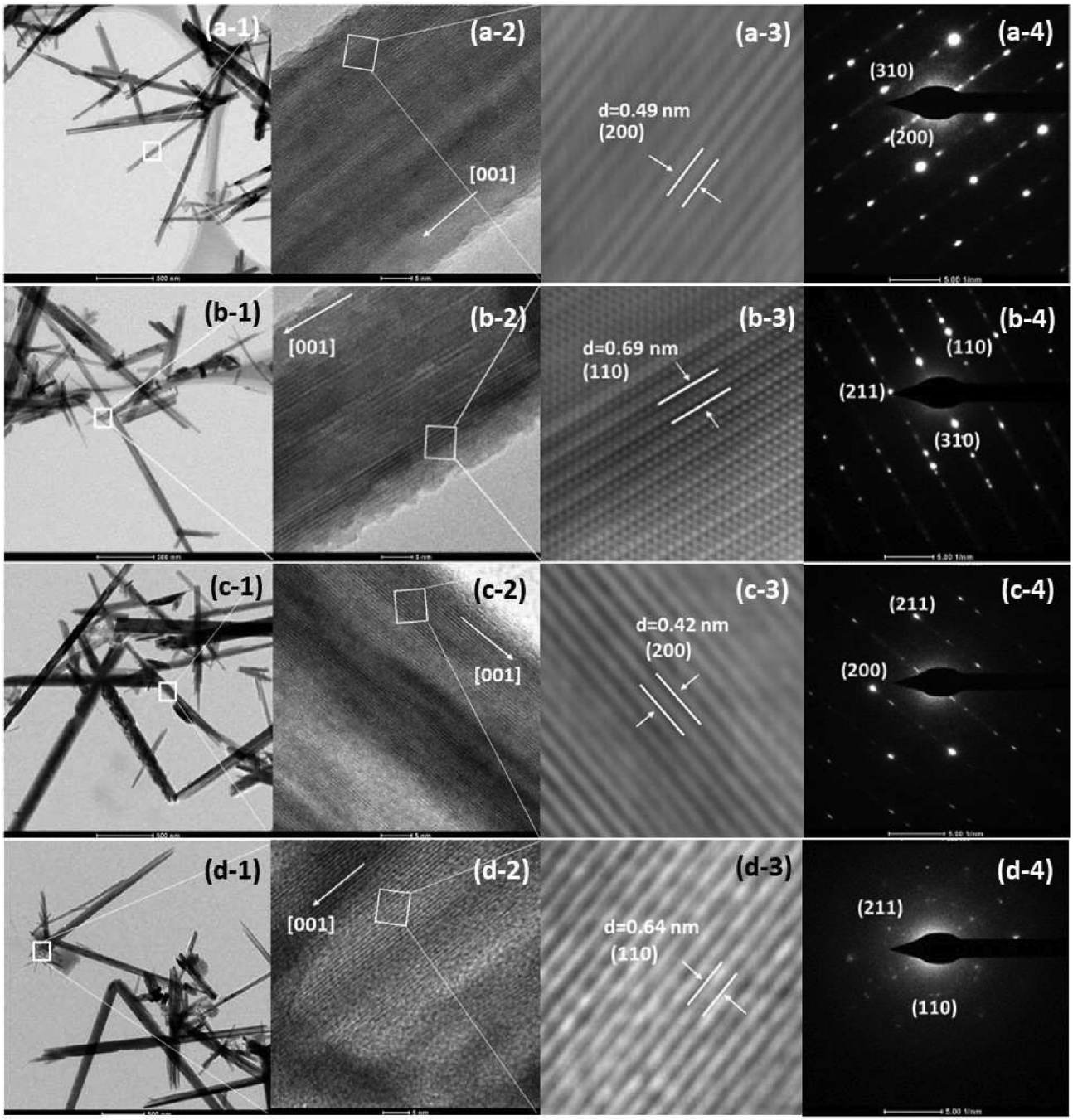

Figure 3. TEM analysis of MCx samples: bright field (a1, b1, c1, d1), HRTEM (a2, b2, c2, d2) (a3, b3, c3, d3) are enlargement of HRTEM and SAED pattern (a4, b4, c4, d4).

compared with the analysis of crystalline size by XRD, the FESEM and TEM results are highly consistent with the size increase with doping percentage. The inaccurate XRD analysis may arise from the nanorod morphology having 54–110 nm in diameter and 2–4 μm in longer which are beyond the validity of the Scherrer formula for size determination.

The HRTEM images in Figure 4(a-3) reveal that the lattice spacing of MC0 is 0.49 nm, which matches the (200) plane of standard α-MnO_2. In addition, the lattice spacing identified as 0.69 nm Figure 4(b-3), 0.42 nm Figure 4(c-3) and 0.64 nm Figure 4(d-3) which corresponds to the reflection plane index (110) (200) and (110). After an evaluation, the lattice parameter of *a-axis* is 9.88, 9.76, 8.36, and 9.05 Å for x = 0, 0.05, 0.10 and 0.15 respectively. These values differ slightly from the XRD data but follow a similar tendency.

The observation of lattice fringes of selected area electron diffraction (SAED) in Figure 3(a-d (4)) confirms the single crystal. It corresponds to the (310) (200) (110), and (211) planes of α-MnO_2 structure and confirms the continuation of tetragonal α-MnO_2 after cation substitution. And consistent with the XRD analysis described earlier.

3.2. *Oxidation state analysis through XANES*

Further investigation on the oxidation state alteration of the manganese and copper during the doping process, ex-situ synchrotron X-ray absorption near-edge spectroscopy (XANES) analysis was performed because of its sensitivity to the local environment around the absorbing atoms. Figure 4 presents XANES of Mn K-edge samples; the reference

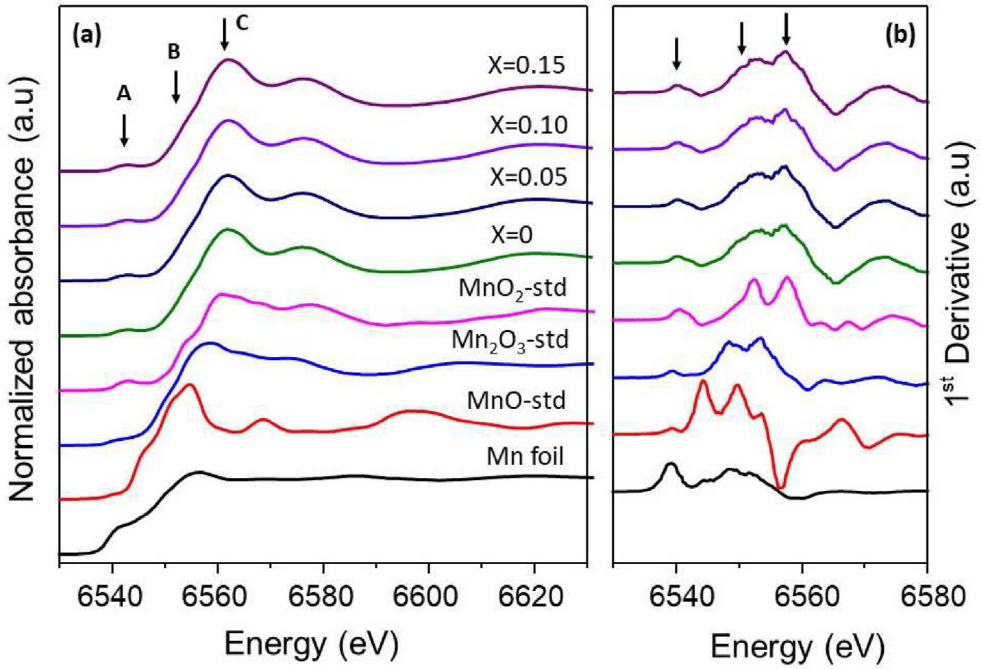

Figure 4. (a) Mn K-edge XANES spectra of MnCx samples, the Mn foil, MnO, Mn_2O_3, and MnO_2 standards are indicated; (b) the First derivative of XANES spectra.

materials Mn foil, MnO, Mn_2O_3, and MnO_2 are presented. The line profiles are assigned to a small pre-edge (A) range of 6540–6545 eV, the primary edge range with shoulder (B) at around 6552 eV, and crest (C) at around 6561 eV that ascribed to a transition from the 1s states to the 4p.

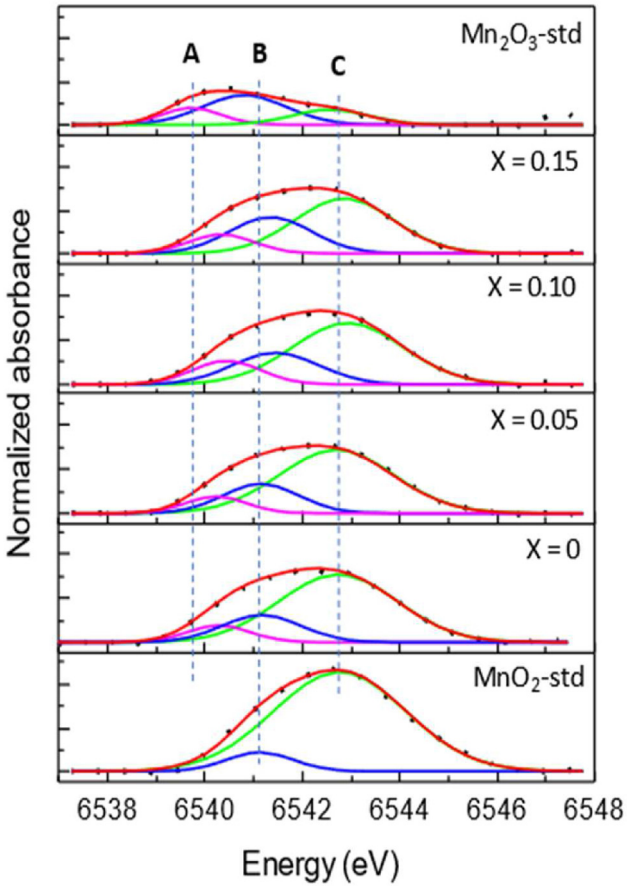

Figure 5. Deconvolution of pre-edge Mn K-edge of MCx samples, the MnO_2, and Mn_2O_3 standard sample spectra are indicated.

The XANES of Mn K-edge in MCx samples slightly differ from the standards. Three main absorptions were distinguished: the pre-edge (A), edge (B), and maximum absorption (C). The weak pre-edge peak is assigned to transition 1s→3d; this transition is formally forbidden but gains intensity through the allowed electric quadrupole transitions; it was split into 1s→3d (t_g) and 1s→3d (e_g). Further analysis of pre-edge absorption through the background removal followed by fitting with Gaussian function and presented in Figure 5. All samples correspond to a pre-edge range comprising three peaks within the energy range 6537–6546 eV varies between Mn_2O_3 and MnO_2 reference, linked to the oxidation state of Mn in MCx samples.

The average oxidation state (AOS) of Mn was taken by the centroid of three components' pre-edge peaks, then compared to the known Mn oxidation states of the standard (MnO_2 and Mn_2O_3), Table 2. When the centroid energy of the standard materials was plotted against oxidation states Mn^{3+} and Mn^{4+}, all the centroid pre-edge peak samples were

Table 2. XANES analysis of MCx average oxidation state (AOS) based on pre-edge of Mn K-edge.

Sample	Pre-edge	Pre-edge area	centroid	AOS
Mn_2O_3-std	6540.45	0.142	6541,54	3
	6542.73	0.096		
	6544.24	0.017		
MnO_2-std	6540.68	0.028	6542.59	4
	6542.56	0.243		
x = 0	6540.57	0.031	6542.18	3.73
	6542.08	0.079		
	6543.50	0.043		
x = 0.05	6540.48	0.025	6542,22	3.78
	6541.68	0.054		
	6543.14	0.077		
x = 0.10	6540.41	0.019	6542.23	3.80
	6541.36	0.032		
	6542.87	0.097		
x = 0.15	6540.51	0.029	6542.11	3.66
	6541.81	0.061		
	6543.19	0.061		

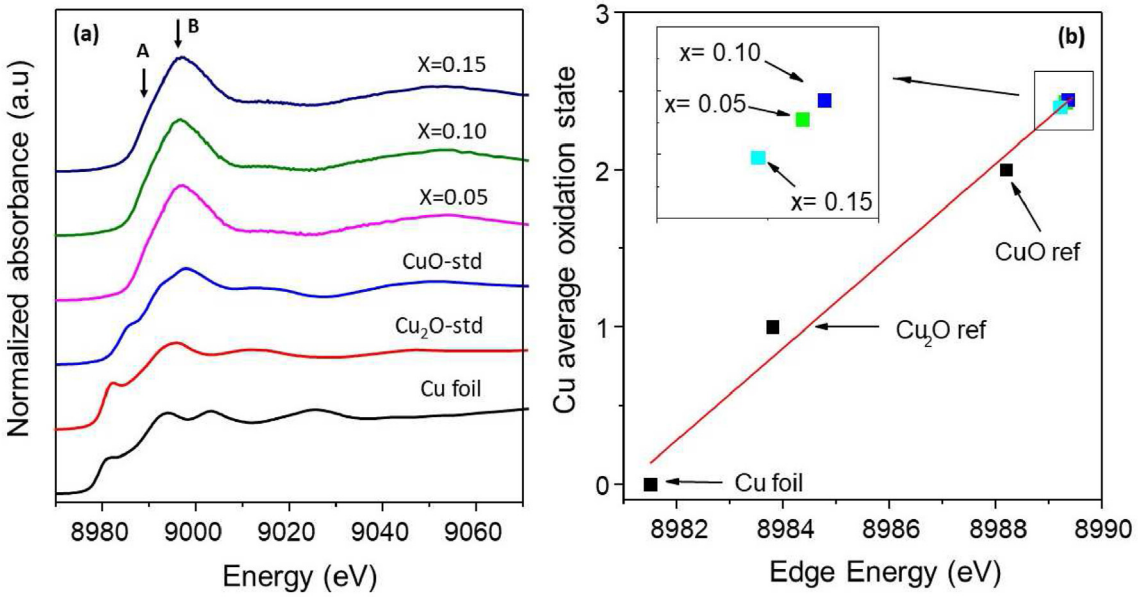

Figure 6. (a) Cu K-edge XANES spectra of MCx sample, Cu foil, CuO, and Cu_2O samples are indicated for reference; (b) AOS of Cu derived from the edge energy Cu K-edge.

within the linear interpolated line and then determined the oxidation state of Mn in questioned, Figure S1. The AOS of Mn is between 3-4, which signifies that the oxidation state is a mixture of Mn^{3+} and Mn^{4+}. The not single oxidation state of Mn distorts the [MnO_6] octahedron and affects both the pre-edge position and the spectral shape. The [MnO_6] octahedron distortion decreases as the Cu dopant increases, shifting the edge towards higher energies, but the contrary occurs at x = 0.15. In the Mn^{4+} with $3d^3$ occupation, three electrons are distributed in the two t_{2g} orbitals, including d_{xy}-d_{xz}, and d_{yz} splitting [40]. For Mn^{3+} ($3d^4$), the t_{2g} orbitals are occupied, and the remaining electron is shared among the e_g orbitals (d_z^2 and d_{x-y}^{22}). The presence of Mn^{3+} and Mn^{4+} in the samples causes a Jahn-Teller distortion of the environment resulting in a modified octahedron symmetry that will be discussed in the EXAFS analysis.

The main absorption range is assigned to dipole transition 1s→4p. The related edge energy is taken as the energy of the peak in the first derivative (Figure 4b), which corresponds to the variation point of the primary edge in the XANES spectra [41]. The spectra for x = 0–0.15 are all remarkably similar but slightly shift toward lower energy which suggests Mn in this sample is in a lower oxidation state. Additionally, the white line region enhancement upon increasing the Cu dopant, particularly at x = 0.15 (C point) compared with MnO_2 reference, indicates that samples contained a higher concentration of edges shared [MnO_6] octahedron that may be stabilized by potassium and copper ions [42].

The absorption edge E_0 shift to lower energy with increasing Cu dopant could be used to obtain the average oxidation state (AOS). The AOS of Mn was determined by establishing a linear relationship between the Mn K-edge energy and Mn oxidation state of reference and comparing

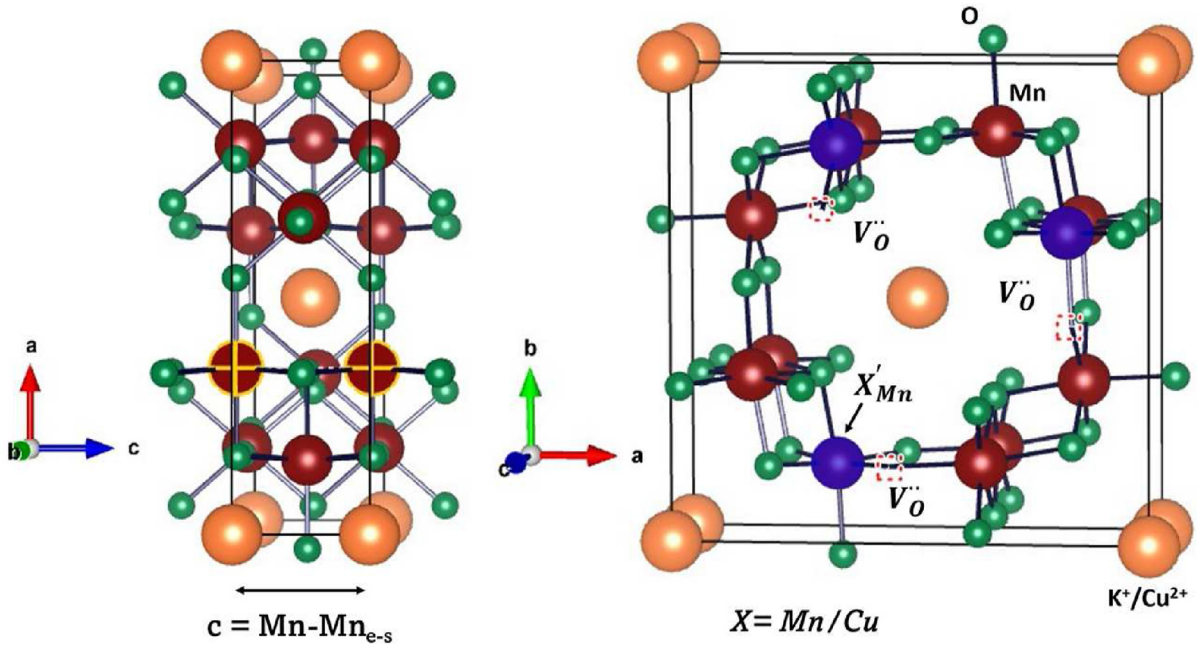

Figure 7. The MnO_2 structure projected on the x-z plane (left) and possible defect structure of $Mn_{1-x}Cu_xO_{2-\delta}$ on the x-y plane (right).

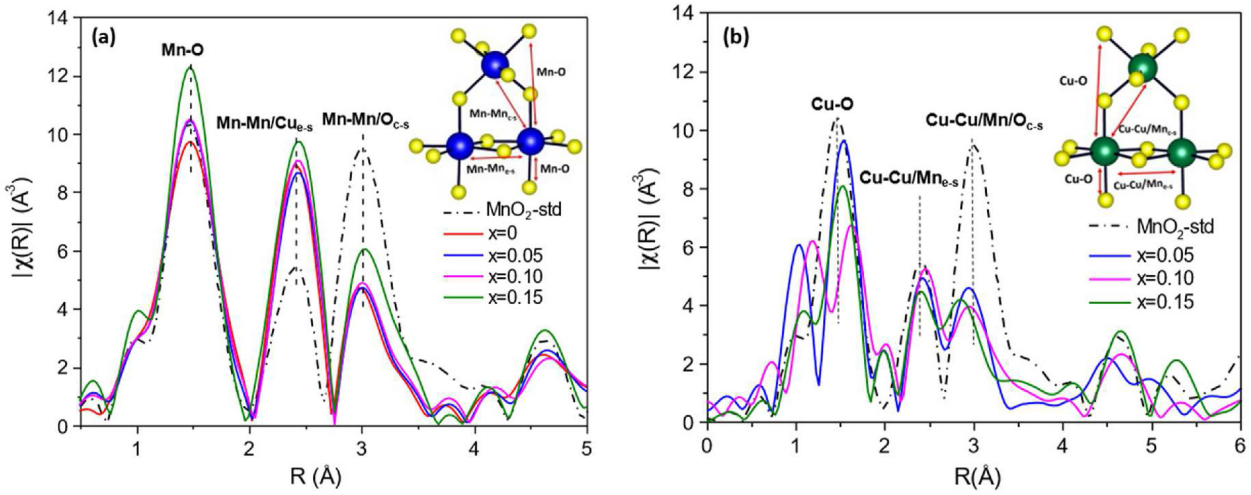

Figure 8. The Fourier transform (FT) magnitudes of the EXAFS spectra: (a) the Mn K-edge of MCx samples and MnO_2 standard; (b) the Cu K-edges of MCx samples and Mn K-edge of MnO_2 standard.

it with samples, Figure S2. The AOS of Mn are 3.71, 3.81, 3.88 and 3.58 for x = 0, 0.05, 0.10 and 0.15, respectively. Further, the XANES data was modeled using standard compounds' linear combination fitting (LCF) data. The two evaluation methods were then combined to approximate Mn's oxidation state, and the samples' relative concentrations are presented in Table S1. From the LCF data, the oxidation state value is almost the same using a linear graph, with the values of 3.65, 3.77, 3.89, and 3.53 for x = 0, 0.05, 0.10, and 0.15, respectively. The weight % of Mn^{3+}/Mn^{4+} at various x is shown in Figure S3. This observation confirms the existence of mixed oxidation states of Mn^{4+} and Mn^{3+} in the samples.

Two possible occurrences may be considered when Cu ions (x = 0–0.15) are present in the MnO2 structure. First, to compensate for the excess negative charge caused by the presence of a Cu ion (Cu^{3+}) at an Mn^{4+} site (Cu'_{Mn}), then oxygen vacancies ($V_O^{\bullet\bullet}$) should be formed. Second, the Jahn-Teller distortion reduces the oxidation state of Mn^{4+} to Mn^{3+} ions ($3d^4$) in octahedron coordination. Besides, the low oxidation state should be addressed to Cu^{2+} partially occupying the tunnel with K ions, causing an increase in Mn^{3+}. This conclusion is consistent with the structure analysis through XRD, where x = 0.15 regain the crystalline volume (Table 1).

Further, oxidation state analysis of Cu ions was carried out using Cu K-edge. Figure 6a shows Cu K-edge XANES spectra of the MCx samples with x = 0.05–0.15 and the standard compounds, Cu foil, Cu_2O, and CuO. The doped samples spectra lost the shoulder type absorption (marked A) compared to the Cu foil, Cu_2O, and CuO (standard compounds) due to the different environment [MnO_6] octahedron. Moreover, the edge energy E_0 shift to a higher value indicates that the copper becomes more oxidized.

For the standards, Cu foils, Cu_2O, and CuO, the edges were found at 8981.50, 8983.80, and 8988.20 eV, respectively, corresponding to a 1s→4p electric dipole transition. The absorption energy of x = 0.05 is 8989.33 eV, while x = 0.10 and 0.15 are 8989.38 and 8989.23 eV. This shift demonstrates the oxidation state of Cu larger than +2 to further determination of Cu oxidation state, the similar method described on the relation of edge energy and oxidation state of Mn described earlier then exploited, Figure 6b. The AOS of Cu varies 2.43, 2.44, and 2.40 for x = 0.05, 0.10 and 0.15 respectively. The decrease in AOS for x = 0.15 is related to the numbers of Cu occupying tunnel possessing low oxidation state Cu^{2+}; otherwise, Cu^{2+} substitutes Mn^{3+} considering the closer ionic radius, 72 pm for Cu^{2+} and 64.5 pm for Mn^{3+}.

Given the previous analysis and the XRD data, it is possible to propose structural defects illustrated in Figure 7. The substitution Cu^{3+} in Mn^{4+} site in [MnO_6] octahedron creates a defect Cu'_{Mn}. The change of the oxidation state of Mn from Mn^{4+}→Mn^{3+} producing defect Mn'_{Mn}, by then Cu^{2+} substitute Mn^{3+} creating a defect Cu'_{Mn}. The excessive Cu^{2+} not accommodated in the octahedron will occupy the tunnel with larger K^+ ions. Those defects cause adjustments in lattice parameters, crystal size, microstrain, oxidation state, lattice distortion, and the formation of defects (oxygen vacancies). The hypothetical defect's reaction is then proposed using the Kroger-Vink notation:

$$2Mn_{Mn}^{x} + Cu_{Cu}^{x} + 5O_O^{x} \rightarrow 2Mn^{3+} + Cu^{2+} + 8e' + 2\frac{1}{2}O_2$$

$$Mn^{3+} + Cu^{2+} \rightarrow Cu'_{Mn}$$

$$Mn^{3+} \rightarrow Mn'_{Mn} + 2V_O^{\bullet\bullet}$$

$$2Mn_{Mn}^{x} + Cu_{Cu}^{x} + 5O_O^{x} \rightarrow Mn'_{Mn} + Cu'_{Mn} + 2V_O^{\bullet\bullet} + 8e' + 2\frac{1}{2}O_2 \quad (2)$$

$$Cu_{Cu}^{x} + O_O^{x} \rightarrow Cu^{3+} + 3e' + \frac{1}{2}O_2$$

$$Cu^{3+} \rightarrow Cu'_{Mn} + 2V_O^{\bullet\bullet}$$

$$Cu_{Cu}^{x} + O_O^{x} \rightarrow Cu'_{Mn} + 2V_O^{\bullet\bullet} + 3e' + \frac{1}{2}O_2 \quad (3)$$

3.3. Local distortion analysis through EXAFS

XRD analysis gives overall data for structure; however, the local aspect of the structure was carried out using the EXAFS data analysis. The magnitudes of the Fourier transformed spectra are shown in Figure S4. The investigation was accomplished by the method of least-squares fitting with the support of ARTHEMIS in IFEFFIT with a parameter of the interatomic distances (R), scattering amplitudes (S_0^2), and Debye-Waller factor (σ^2). As can be seen clearly from the Fourier transforms (FTs) of Mn K-edge EXAFS spectra in Figure 8a, all MCx samples display three intense peaks, which correspond to the (Mn–O) (Mn–Mn/Cu)$_{e-s}$, and (Mn–Mn/O)$_{c-s}$ bonding pairs, respectively. The Mn K-edge EXAFS spectra are well-reproduced with α-MnO_2 structure, with insignificant peak shifts.

The relative peak intensity of the Mn–O and Mn–Mn in the Fourier transformed EXAFS is strongly affected by the cation arrangements in the MnO_2 structure. The standard MnO_2 poses high intensity in χ(R) of the Mn–O peak of the first shell and low intensity of the Mn–Mn peak of the

Table 3. Interatomic distances R of the Mn absorber to its neighbors of MCx samples, the MnO_2 standard is indicated for reference.

Sample	Shell	Bonding	CN	R (Å)	σ^2	S_o^2	R-factor
MnO_2-std	1	Mn–O	6	1.87	0.006	0.708	0.0285
	2	Mn–Mn	4	2.90	0.010		
	3	Mn–O	7	3.72	0.004		
		Mn–Mn	4	3.43	0.002		
x = 0	1	Mn–O1	3.24 ± 0.75	1.88 ± 0.03	0.002	0.708	0.0194
		Mn–O2	1.67 ± 0.75	1.92 ± 0.06	0.002		
	2	Mn–Mn	4	2.89 ± 0.01	0.004		
	3	Mn–O	5.25 ± 3.62	3.54 ± 0.06	0.003		
		Mn–Mn	4	3.43 ± 0.02	0.003		
x = 0.05	1	Mn–O1	3.18 ± 0.79	1.87 ± 0.04	0.002	0.708	0.0198
		Mn–O2	1.64 ± 0.79	1.91 ± 0.08	0.002		
	2	Mn–Mn	3.41 ± 0.22	2.87 ± 0.09	0.005		
		Mn–Cu	0.62 ± 0.15	2.81 ± 0.84	0.003		
	3	Mn–O	6.75 ± 2.45	3.38 ± 0.07	0.002		
		Mn–Mn	4	3.41 ± 0.09	0.002		
x = 0.10	1	Mn–O1	3.33 ± 0.92	1.87 ± 0.06	0.003	0.708	0.0205
		Mn–O2	1.71 ± 0.92	1.90 ± 0.09	0.002		
	2	Mn–Mn	3.06 ± 0.36	2.88 ± 0.12	0.005		
		Mn–Cu	1.02 ± 0.24	2.82 ± 0.47	0.003		
	3	Mn–O	6.87 ± 2.63	3.39 ± 0.08	0.003		
		Mn–Mn	4	3.40 ± 0.07	0.001		
x = 0.15	1	Mn–O1	3.52 ± 0.05	1.88 ± 0.05	0.002	0.708	0.0187
		Mn–O2	1.81 ± 0.05	1.86 ± 0.11	0.003		
	2	Mn–Mn	2.60 ± 0.26	2.88 ± 0.02	0.003		
		Mn–Cu	1.61 ± 0.29	2.81 ± 0.02	0.003		
	3	Mn–O	6.97 ± 3.04	3.41 ± 0.06	0.003		
		Mn–Mn	4	3.40 ± 0.03	0.006		

second shell. This intensity is weaker than the third shells of Mn–O/Mn–Mn, Figure 8a. When Cu dopant is incorporated in MnO_2, Mn is replaced by a heavier Cu ion, which has strong electron scattering power; therefore, the Mn–Cu peak becomes much stronger relative to the Mn–Mn standard [37]. In contrast, decreasing intensity Mn–O peaks at the third shell indicate the existence of oxygen vacancies in the MnO_2 structure. The copper substitution induced charged defect Cu'_{Mn} and neutralization creates oxygen vacancy $V_O^{\bullet\bullet}$. The fitting process is carried out using the ARTHEMIS software to demonstrate the presence of oxygen vacancy. It was determined first through MnO_2 standard fitting by fixed CN, then used for fitting other samples.

The numerical values of oxygen up to the third shell are presented in Table 3. Assuming the standard MnO_2 has no oxygen vacancy possessing 13 oxygen in this cluster, therefore, the relative oxygen vacancy should be determined *i.e.*, 21.8 %, 11.0 %, 8.4 %, 8.5 % for x = 0, 0.05, 0.10, 0.15, respectively. These values are believed to be strongly related to the oxidation state of Mn, which has been discussed in the previous XANES analysis. Furthermore, focusing on the Mn–O distances in the first shell demonstrates a distortion along the c-axis, *i.e.*, the octahedron [MnO_6] becoming elongated (the distance of Mn–O2 is longer than Mn–O1 shells) for x = 0–0.10 while compressed for x = 0.15. In the second and third shell, the distances of Mn absorber to Mn/Cu/O are shortened, which

Table 4. Interatomic distances R of the Cu absorber to the first neighbor O octahedron, second neighbor Mn/Cu, and third neighbor Mn/Cu and O of MCx samples.

Sample	Shell	Bonding	CN	R (Å)	σ^2	S_o^2	R-factor
x = 0.05	1	Cu–O1	3.36 ± 0.19	2.00 ± 0.02	0.001	0.708	0.0552
		Cu–O2	1.68 ± 0.19	1.91 ± 0.05	0.002		
	2	Cu–Mn	4	2.89 ± 0.04	0.014		
	3	Cu–O	3.88 ± 1.16	3.28 ± 0.20	0.02		
		Cu–Mn/Cu	4	3.41 ± 0.03	0.006		
x = 0.10	1	Cu–O1	2.45 ± 0.09	2.04 ± 0.02	0.001	0.708	0.0323
		Cu–O2	1.22 ± 0.09	1.50 ± 0.02	0.001		
	2	Cu–Mn	4	2.98 ± 0.03	0.009		
	3	Cu–O	6.65 ± 0.79	3.61 ± 0.08	0.007		
		Cu–Mn	4	3.49 ± 0.04	0.004		
x = 0.15	1	Cu–O1	3.50 ± 0.87	2.00 ± 0.02	0.002	0.708	0.0441
		Cu–O2	1.81 ± 0.87	1.89 ± 0.03	0.001		
	2	Cu–Mn	4	2.92 ± 0.05	0.018		
	3	Cu–O	3.91 ± 0.51	3.24 ± 0.06	0.002		
		Cu–Mn	4	3.41 ± 0.07	0.006		

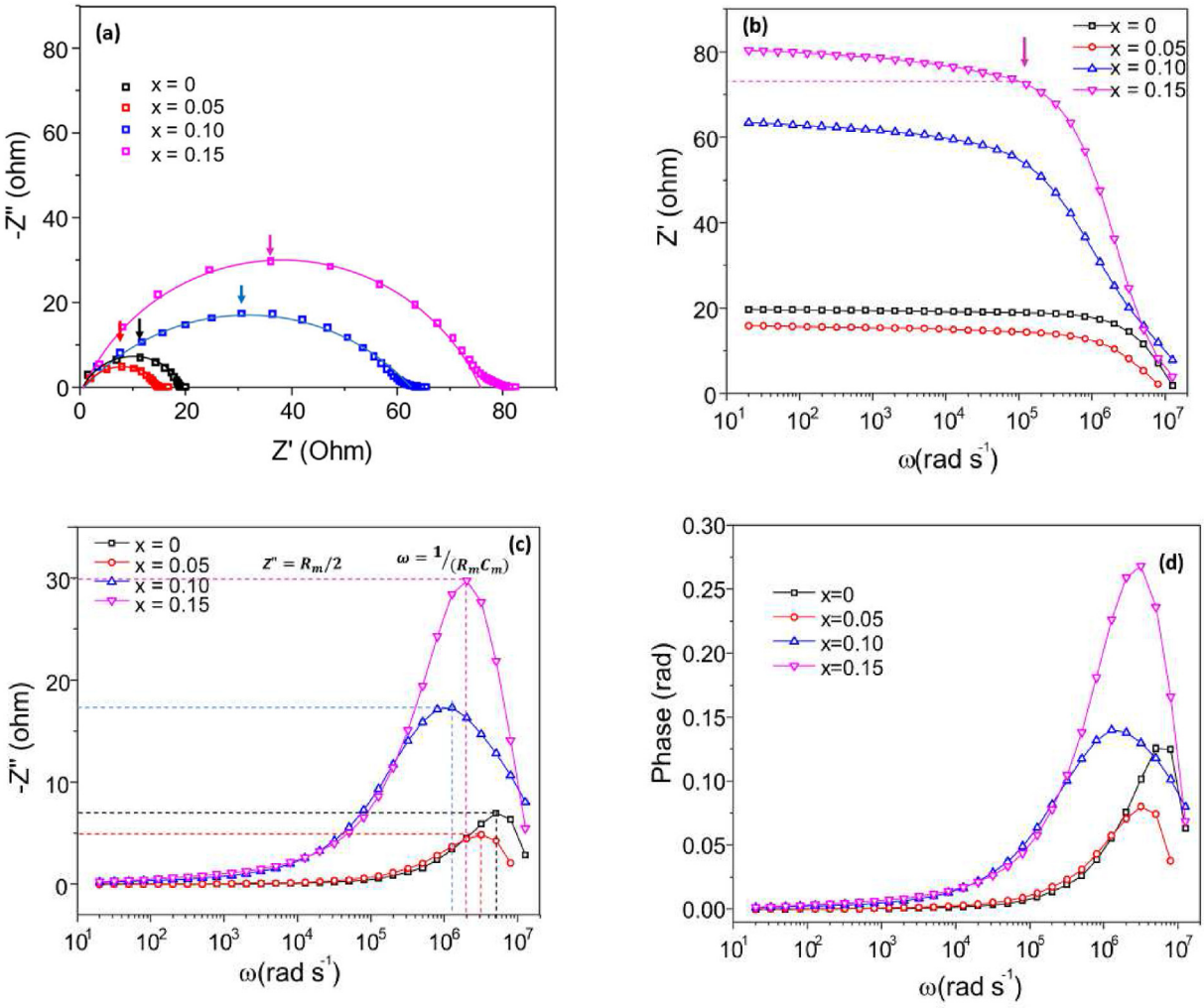

Figure 9. (a) Nyquist plot of real impedance Z′ versus imaginary impedance Z′′; and angular frequency dependence of (b) Real impedance *Z*' (c) imaginary impedance *Z*'' and (d) phase of impedance.

signify a reduction of the lattice volume, as was discussed by XRD analysis in the previous section.

The detailed local structure information around the Cu absorber on the Cu-doped samples was elucidated using Cu K-edge. Figure 8b shows the Fourier transform (FT) EXAFS spectra of MCx at the Cu K-edges and MnO_2 standard at the Mn K-edge. The spectra of Cu K-edge of MCx and Mn K-edge of MnO_2 standard exhibit a similar trend, particularly the energy position, suggesting that Mn and Cu have similar octahedron environments, demonstrating Cu substitute Mn. Given the XRD data, in which no other phase was detected except α-MnO_2, the further fitting procedure utilized the MnO_2 model structure; the results are listed in Table 4. Cu's coordination number (CN) in the first shell is lower than 6, the ideal octahedron [CuO_6]. While their distance is not similar, demonstrating that the octahedron is distorted.

Furthermore, the intensity of Cu–O is lower than that of the Mn–O standard displaying a lower number of Cu–O interactions. A similar manner is presented in the third shell, which indicates a very significant decrease in the intensity of the Cu–O interaction. The second shell can be assigned to Cu–Cu bonds and shows a similar characteristic with an intensity of Mn–Mn standard peaks, confirming that the doped Cu ions substitute Mn in the octahedron, as stated earlier.

Given the data presented in Tables 3 and 4, the distorted octahedron [MO6] is elongated for x = 0–0.10 and compressed for x = 0.15. Noticed that the elongated octahedron on the x = 0 sample should be attributable to the existing K^+ causing the rendering $Mn^{4+} \rightarrow Mn^{3+}$. On the other hand, since the oxidation state analysis presented earlier, the splitting of either d_{xy}-d_{xz}, d_{yz} or d_z^2, d_{x-y}^{22} is associated with the Jahn Teller effect, Figure S5.

Table 5. Grains resistance R_m and capacitance C_m of α-MnO_2 derived from Nyquist and Debye plots.

Sample	R_m (ohm)		C_m (nF)	
	'Nyquist'	'Debye'	'Nyquist'	'Debye'
x = 0	20	16	10.0	12.5
x = 0.05	12	10	26.5	33.3
x = 0.10	45	36	17.6	23.1
x = 0.15	60	60	8.3	8.3

3.4. Electrical properties

The electrical analysis should proceed through two approaches, *Z*' – *Z*'' the Nyquist plot and the Debye plot [43]. The Nyquist plot of real impedance Z′ versus imaginary impedance Z″ was generally modeled consisting of shunt wiring circuit, semicircles of grains response, and other tail at low frequency as electrode responses. Focusing on the grains response, wires, and electrode data should be omitted; consequently, the frequency range used for further analysis is 1 Hz–2 MHz (≈10 rad s^{-1} – 10^7 rad s^{-1}), Figure 9.

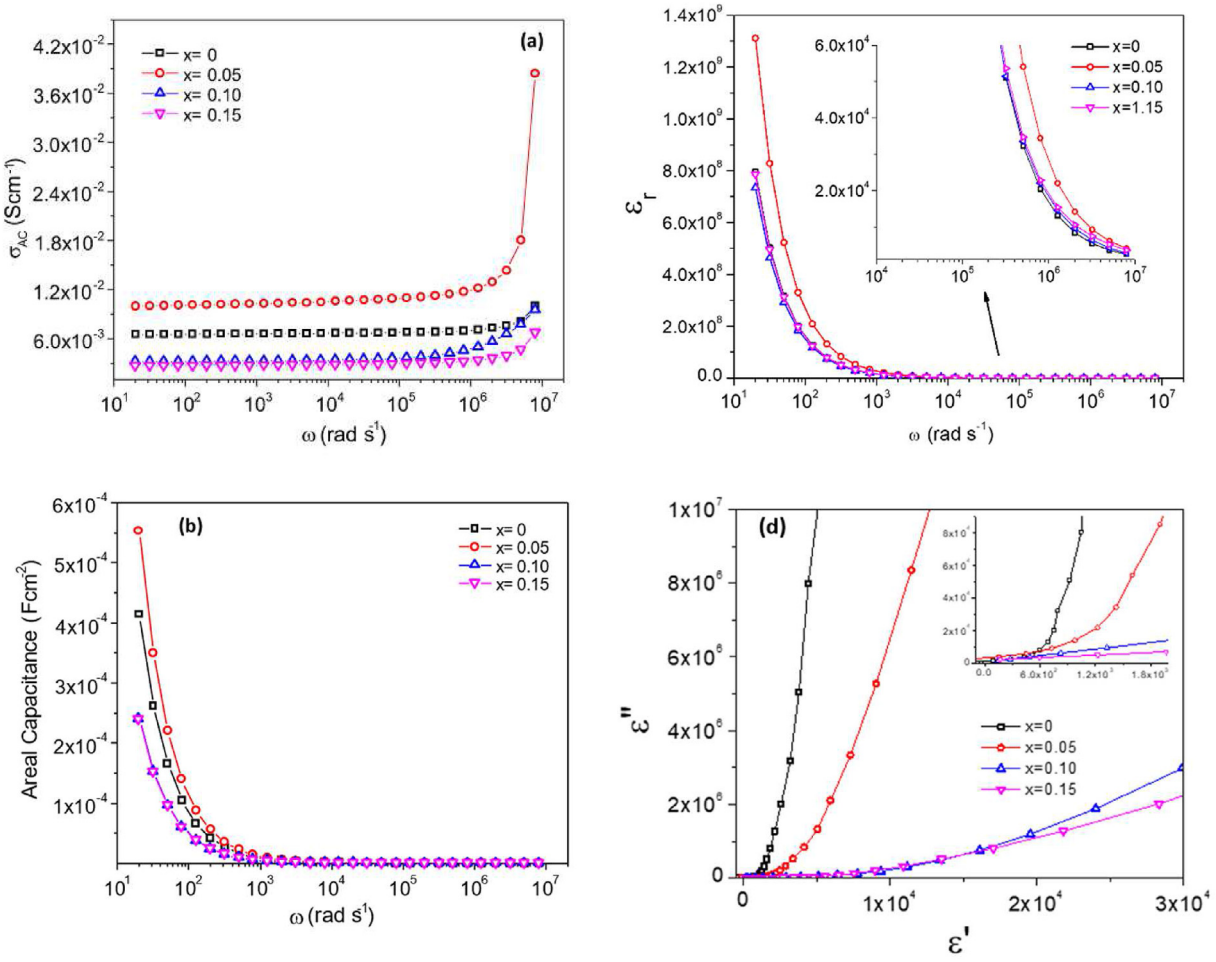

Figure 10. (a) The dependency angular frequency ω on AC conductivity; (b) The dependency angular frequency ω on areal capacitance; (c) The dependency of angular frequency on relative permittivity ε_r; and (d) Complex plane plot of ε'- ε'' for MCx samples.

Utilizing the reduced data described previously, a decrease in the semicircle size in the MC0.05 doping sample indicated better grain conductivity. The semicircle radius increased in MC0.10 and MC0.15 samples. The grains resistance (R_m) and capacitance (C_m) of the sample were estimated based diameter of a semicircle of the Z' - Z'' response, Table 5.

Moreover, Figure 9b represents the real Z′ impedance component against angular frequency; the Z′ amplitude is higher in the low low-frequency region and decreases monotonically with increasing frequency, then a significant decline above $\omega \approx 10^5$ rad s^{-1}. The frequency dependence of imaginary impedance Z″ at various dopant concentrations is represented in Figure 9c, showing a typical Debye 'relaxation' curve above $\omega = 10^5$ rad s^{-1} at the zone of Z' decline. A similar fashion for the phase of impedance ($arc\tan(-Z''/Z')$) is shown in Figure 9d. Further detailed numerical values of R_m and C_m determined through relaxation frequency, focussing on the grains response the Z' and Z'' should be presented as follows [44]:

$$Z' = \frac{R_m}{1 + (\omega R_m C_m)^2} \tag{4}$$

$$-Z'' = R_m \frac{\omega R_m C_m}{1 + (\omega R_m C_m)^2} \tag{5}$$

At the relaxation $\omega = \frac{1}{R_m C_m}$, then deduced the numerical value of the resistance and capacitance of the material, Table 5.

The charges influence the overall sample conductivity against frequency, and the defect mobility is determined by defect reactions (Eqs. (2) and (3)) as presented in Figure 10a was calculated following equation [43].

$$\sigma_{AC} = \frac{d}{A}\left(\frac{Z'}{Z'^2 + Z''^2}\right) \tag{6}$$

It shows that the behavior is quasi-frequency-independent in the low-frequency region (up to $\omega = 10^5$ rad s^{-1}) and follows the Debye relaxation curve above $\omega = 10^5$ rad s^{-1}. At room temperature, the mobility of possible ionic defects presents in the MCx samples Mn'_{Mn}, Cu'_{Mn}, K^+, Cu^{2+} are much smaller than the mobility of electrons e'; therefore, the electrons dominate the sample conductivity. Given the defect reaction in (2(2) and (3)(3), the conductivity of MCx samples can be described as the following: (i) The high conductivity of the MC0 sample is related to the K^+ incorporated in the tunnel. (ii) The conductivity MC0.05 sample increases due to the possibility of copper exhibiting two diverse oxidation states. The determinant factor is related to Cu^{2+} substitute Mn^{3+} creating 8 e' and Cu^{3+} substitute Mn^{4+} creating 3 e' in the octahedron. In the beginning, the Cu^{2+} creating 8 e' will dominate the conductivity, afterward depending on the quantity of copper presenting oxidation state. Therefore, the small number of Cu dopants resulted in better conductivity. (iii) For high dopant (x = 0.10, 0.15), the number of Cu^{3+} becomes numerous, considering that the Cu^{3+} create 3 e' (eq. 3) then has an effect worsening conductivity.

Figure 10b records the areal capacitance as a function of the frequency of various Cu doped MnO_2, revealing differences between samples, with the highest values of MC0.05 sample. The remarkably high areal capacitance at low frequency, mainly the response of space charges and decreases sharply with increasing frequency, is caused by the polarization response. The areal capacitance of the sample has directly related to the permittivity of the material. Further examination of permittivity is then intriguing. Figure 10c shows the relative permittivity as a function of angular frequency at various doping levels. The dielectric constant of all samples was found to decrease with increasing frequency before reaching nearly constant values in the high-frequency region. The relative permittivity at low frequency is determined by space charge, while high frequency is determined by dipole polarization. The space charges are the unbounded electrons created after a defect reaction induced to exceptionally high relative permittivity. The inhomogeneous defect structure due to the presence of multiple defects in the material ($Cu'_{Mn}, Mn'_{Mn}, Mn''_{Mn}, V_O^{\bullet\bullet}$) that derive the formation of defect dipoles, which leap to face the external electric field's high frequency, resulting in low permittivity. Figure 10d reveals the complex plane plot of ε'- ε'', which lacks the Debye relaxation type curve; this indicates that the material is rather ionic than a standard dielectric. Given the frequency used in this analysis ($\omega \approx 10$–10^7 rad s^{-1}), the dipole and space charge dominates the properties. The shifting of dipole transition to space charge shape to higher ε' for increasing Cu dopant witnessed the defect dipole created when Cu dopant was incorporated in the material.

4. Conclusion

The composition $Mn_{1-x}Cu_xO_2$ (x = 0–0.15) has been synthesized through hydrothermal processes and characterized. XRD analysis revealed that all samples hold α-MnO_2 type structure (JCPDS 44–0141) and I4/m symmetry, while FESEM shows nanorods morphology and their size increase with dopant percentage. The oxidation state of manganese is a mixture of 3+ and 4+, which drag the formation of defects $Mn'_{Mn}, V_O^{\bullet\bullet}, e'$. Adding Cu doping on Mn1-xCuxO2 causes lattice parameters and crystal size rearrange. The AOS of copper in MCx samples determined through XANES was more than 2+. It signifies Cu^{2+} and Cu^{3+}. The Cu^{2+} tends to substitute Mn^{3+} and possibly in the tunnel considering its size. Finally, Cu^{3+} replaces Mn^{4+} in the octahedron. The placement of multivalence Cu either substitute Mn or incorporated in the tunnel results in the formation of multiple defects, including Cu'_{Mn}, $Cu^x_{Mn}, Mn'_{Mn}, V_O^{\bullet\bullet}$, e', elongated and compressed the Jahn Teller effect. Electrical characterization at room temperature revealed that the conductivity of Cu-doped MnO_2 is dominated by electrons and influenced by the various oxidation state of the cations in the octahedron sites, *viz.* defects: Cu'_{Mn}, $Cu^x_{Mn}, Mn'_{Mn}, V_O^{\bullet\bullet}$ and the movement of large K^+ ions in the tunnel. The maximum conductivity achieved by x = 0.05 present $R_g = 10\ \Omega$, generate AC conductivity 2.3×10^{-3} S m^{-1} at low frequency. While the dielectric constant ε_r at a low frequency is controlled by space charge and disappears at high frequency when dipole due to defect becoming dominant. The areal capacitance declines with frequency and attains the maximum given by the MC0.05 sample. These conclude that Cu dopant increase

Declarations

Author contribution statement

E. Hastuti: Conceived and designed the experiments; Performed the experiments; Analyzed and interpreted the data; Wrote the paper.

A. Subhan, P. Amonpattaratkit: Performed the experiments; Analyzed and interpreted the data.

M. Zainuri, T. Triwikantoro: Conceived and designed the experiments; Analyzed and interpreted the data; Wrote the paper.

S. Suasmoro: Conceived and designed the experiments; Performed the experiments; Analyzed and interpreted the data; Contributed reagents, materials, analysis tools or data; Wrote the paper.

Funding statement

This research did not receive any specific grant from funding agencies in the public, commercial, or not-for-profit sectors.

Data availability statement

Data will be made available on request.

Declaration of interests statement

The authors declare no conflict of interest.

Additional information

Supplementary content related to this article has been published online at https://doi.org/10.1016/j.heliyon.2022.e11459.

Acknowledgements

This research is supported by the Indonesian Ministry of Research and Higher Education through the World Class Research program managed by DPRM ITS contract No: 1042/PKS/ITS/2021. The authors would like to thank Research Centre for Physics LIPI for utilizing Microscopy Facilities and the SUT-NANOTEC-SLRI -BL8 joint research facility for synchrotron utilization, Thailand, for XAS beam time.

References

[1] J. Liu, J. Wang, C. Xu, H. Jiang, C. Li, L. Zhang, et al., Advanced energy storage devices: basic principles, analytical methods, and rational materials design, Adv. Sci. 1700322 (2018) 5.
[2] Wang B. Nanostructured transition metal oxide materials for supercapacitor application n.d.:106.
[3] P. Forouzandeh, V. Kumaravel, S.C. Pillai, Electrode materials for supercapacitors: a review of recent advances, Catalysts 969 (2020) 10.
[4] C. Du, N. Pan, Carbon Nanotube-Based Supercapacitors, 2007, pp. 4–8.
[5] A.G. Pandolfo, A.F. Hollenkamp, Carbon properties and their role in supercapacitors, J. Power Sources 157 (2006) 11–27.
[6] I.V. Barsukov, C.S. Johnson, J.E. Doninger, V.Z. Barsukov (Eds.), New Carbon Based Materials for Electrochemical Energy Storage Systems: Batteries, Supercapacitors and Fuel Cells, 229, Springer Netherlands, Dordrecht, 2006.
[7] Y. Huang, J. Liang, Y. Chen, An overview of the applications of graphene-based materials in supercapacitors, Small 8 (2012) 1805–1834.
[8] M. Jayalakshmi, K. Balasubramanian, Simple capacitors to supercapacitors—an overview, Int. J. Electrochem. Sci. 3 (2008) 22.
[9] Y. Wang, J. Guo, T. Wang, J. Shao, D. Wang, Y.-W. Yang, Mesoporous transition metal oxides for supercapacitors, Nanomaterials 5 (2015) 1667–1689.
[10] A. González, E. Goikolea, J.A. Barrena, R. Mysyk, Review on supercapacitors: technologies and materials, Renew. Sustain. Energy Rev. 58 (2016) 1189–1206.
[11] Christian Julien, Alain Mauger, Nanostructured MnO_2 as electrode materials for energy storage, Nanomaterials 396 (2017) 7.
[12] D.P. Dubal, P. Gómez-Romero, Metal oxides in supercapacitors, 2017.
[13] Y. Yuan, L. Ma, K. He, W. Yao, A. Nie, X. Bi, et al., Dynamic study of (De)sodiation in alpha-MnO_2 nanowires, Nano Energy 19 (2016) 382–390.
[14] D.P. Dubal, R. Holze, Synthesis, properties, and performance of nanostructured metal oxides for supercapacitors, Pure Appl. Chem. 86 (2014) 611–632.
[15] T. Xiong, Y. Zhang, W.S.V. Lee, J. Xue, Defect engineering in manganese-based oxides for aqueous rechargeable zinc-ion batteries: a review, Adv. Energy Mater. 2001769 (2020) 10.
[16] Y. Wang, Y.-Z. Zhang, Y.-Q. Gao, G. Sheng, J.E. ten Elshof, Defect engineering of MnO_2 nanosheets by substitutional doping for printable solid-state micro-supercapacitors, Nano Energy 68 (2020) 104306.
[17] M.U. Khalid, M.F. Warsi, I. Shakir, M.F. Aly Aboud, M. Shahid, S.S. Shar, et al., Al^{3+}/Ag^{1+} induced phase transformation of MnO_2 nanoparticles from α to β and their enhanced electrical and photocatalytic properties, Ceram. Int. 46 (2020) 9913–9923.
[18] Y. Xiao, W. Huo, S. Yin, D. Jiang, Y. Zhang, Z. Zhang, et al., One-step hydrothermal synthesis of Cu-doped MnO_2 coated diatomite for degradation of methylene blue in Fenton-like system, J. Colloid Interface Sci. 556 (2019) 466–475.

[19] S. Fu, L. Li, Y. Jing, Y. Zhang, X. Wang, S. Fang, et al., Crystal growth of bimetallic oxides $CuMnO_2$ with tailored valence states for optimum electrochemical energy storage, Cryst. Growth Des. 18 (2018) 6107–6116.

[20] A. Zahoor, H.S. Jang, J.S. Jeong, M. Christy, Y.J. Hwang, K.S. Nahm, A comparative study of nanostructured α and δ MnO_2 for lithium oxygen battery application, RSC Adv. 4 (2014), 8973.

[21] C. Kahattha, S. Santhaveesuk, Influence of calcination temperature on physical and electrochemical properties of MnO_2 nanoparticles synthesized by co-precipitation method, Ferroelectrics 552 (2019) 121–131.

[22] T.M. Benedetti, V.R. Gonçales, D.F.S. Petri, Torresi SIC de, Torresi RM. Macroporous MnO_2 electrodes obtained by template assisted electrodeposition for electrochemical capacitors, J. Braz. Chem. Soc. 21 (2010) 1704–1709.

[23] F. Hashemzadeh, M. Mehdi Kashani Motlagh, A. Maghsoudipour, A comparative study of hydrothermal and sol–gel methods in the synthesis of MnO_2 nanostructures, J. Sol. Gel Sci. Technol. 51 (2009) 169–174.

[24] S.-L. Chiam, S.-Y. Pung, F.-Y. Yeoh, Recent developments in MnO_2-based photocatalysts for organic dye removal: a review, Environ. Sci. Pollut. Res. 27 (2020) 5759–5778.

[25] X. Zhao, Y. Hou, Y. Wang, L. Yang, L. Zhu, R. Cao, et al., Prepared MnO_2 with different crystal forms as electrode materials for supercapacitors: experimental research from hydrothermal crystallization process to electrochemical performances, RSC Adv. 7 (2017) 40286–40294.

[26] X. Li, J. Ma, L. Yang, G. He, C. Zhang, R. Zhang, et al., Oxygen vacancies induced by transition metal doping in γ-MnO_2 for highly efficient ozone decomposition, Environ. Sci. Technol. 52 (2018) 12685–12696.

[27] M. Wang, L. Árnadóttir, Z.J. Xu, Z. Feng, Situ X-ray absorption spectroscopy studies of nanoscale electrocatalysts, Nano-Micro Lett. 11 (2019).

[28] A. Gaur, B.D. Shrivastava, A comparative study of the methods of speciation using X-ray absorption fine structure, Acta Phys. Pol., A 121 (2012) 647–652.

[29] A. Kuzmin, J. Chaboy, EXAFS and XANES analysis of oxides at the nanoscale, IUCrJ 1 (2014) 571–589.

[30] C.H.M. van Oversteeg, H.Q. Doan, F.M.F. de Groot, T. Cuk, In situ X-ray absorption spectroscopy of transition metal based water oxidation catalysts, Chem. Soc. Rev. 46 (2017) 102–125.

[31] F. Fitriana, P.S.N. Baity, M. Zainuri, P. Kidkhunthod, S. Suasmoro, Crystal structure and Cu/Fe K-edge analysis of $Ba_{0.5}Sr_{0.5}Fe_{1-x}Cu_xO_{3-\delta}$ (x = 0–0.2) and the influence on conductivity, J. Phys. Chem. Solid. 154 (2021), 110065.

[32] F. Latief, M. Absa, M. Andansari, M.A. Baqiya, P. Kidkhunthod, S. Suasmoro, Structure and local structure investigation of $(0.85\text{-}x)BaTiO_3\text{-}0.15BiFeO_{3-x}KVO_3$ system linked to electrical properties, Mater. Chem. Phys. 276 (2022), 125414.

[33] E. Hastuti, W.R. Agustin, I. Yuliana, Effect of doping Fe^{3+} and Cu^{2+} on the microstructure and electrical properties of cryptomelane-type MnO_2 prepared by sol-gel method, IOP Conf. Ser. Earth Environ. Sci. 456 (2020), 12017.

[34] Ferreira T, Rasband W. ImageJ user guide n.d.:198.

[35] V. Grillo, Advances in STEM-CELL. A free software for TEM and STEM analysis and simulations: probe deconvolution in STEM-HAADF, Microsc. Microanal. 17 (2011) 1292–1293.

[36] M. Klinger, More features, more tools, more *CrysTBox*, J. Appl. Crystallogr. 50 (2017) 1226–1234.

[37] B. Ravel, M. Newville, ATHENA and ARTEMIS interactive graphical data analysisusing IFEFFIT, Phys. Scripta 1007 (2005).

[38] U. Nuraini, D. Agustianawati, E. Yahya, Y. Cahyono, P. Kidkhunthod, S. Suasmoro, The influence of local distortion on the electrical properties of the $(1\text{-}x)(K_{0.5}Na_{0.5})NbO_{3-x}(Ba_{0.8}C_{0.2})TiO_3$ system, Ceram. Int. 43 (2017) 3664–3669.

[39] B.D. Cullity, Elements of X-ray Diffraction, 2d ed., Mass: Addison-Wesley Pub. Co, Reading, 1978.

[40] F. Wunderlich, T. Leisegang, T. Weißbach, M. Zschornak, H. Stöcker, J. Dshemuchadse, et al., EXAFS, XANES, and DFT study of the mixed-valence compound YMn_2O_5 : site-selective substitution of Fe for Mn, Phys. Rev. B 82 (2010).

[41] P. Gao, P. Metz, T. Hey, Y. Gong, D. Liu, D.D. Edwards, et al., The critical role of point defects in improving the specific capacitance of δ-MnO_2 nanosheets, Nat. Commun. 8 (2017).

[42] S.-J. Hwang, C.-W. Kwon, J. Portier, G. Campet, H.-S. Park, J.-H. Choy, et al., Local crystal structure around manganese in new potassium-based nanocrystalline manganese oxyiodide, J. Phys. Chem. B 106 (2002) 4053–4060.

[43] S. Nasri, A.L. Ben Hafsia, M. Tabellout, M. Megdiche, Complex impedance, dielectric properties and electrical conduction mechanism of $La_{0.5}Ba_{0.5}FeO_{3-\delta}$ perovskite oxides, RSC Adv. 6 (2016) 76659–76665.

[44] Heath JP. Simulation of impedance spectroscopy in electroceramics using a finite element method n.d.:207.